# GPR investigations for the study and the restoration of the rose window of Troia Cathedral (southern Italy)

Nicola Masini[1,2], Luigia Nuzzo[3*] and Enzo Rizzo[4]

[1] *Institute of Archeological Heritage – Monuments and Sites, IBAM-CNR – Lagopesole (PZ), Italy*

[2] *DAPIT, University of Basilicata, Potenza, Italy*

[3] *Department of Materials Science, University of Lecce, Via per Arnesano, Lecce 73100, Italy*

[4] *Institute of Methodologies for the Environmental Analysis, IMAA-CNR, Tito Scalo (PZ), Italy*

## ABSTRACT

The development of cracks and distortions caused by past seismic events compromised the integrity of the rose window of Troia Cathedral, one of the most precious Romanesque monuments in southern Italy. Ground-penetrating radar (GPR) using high-frequency antennae (mainly 1500 MHz) was selected from among various non-destructive testing methods for its high-resolution imaging to scan the internal structure of the various architectural elements of the wheel window: the decimetre-diameter columns constituting the rays, the ring decorated with intersecting arched ribwork and the surrounding circular ashlar curb. GPR was employed in the classical continuous reflection mode, moving the antennae manually along the architectural elements and paying exceptional care in the acquisition and processing stages to avoid positioning errors. Indeed, the challenging aspects of this case study were the geometrical complexity and small dimensions of the structural elements, causing many logistic/coupling problems. In spite of this, through proper interpretation techniques, based on signal analysis (presence of reflections and diffractions, velocity and attenuation variations) and correlation with features detected by visual inspection of the external surfaces, the GPR survey provided useful information on the internal structure of the rose window, detecting fractures and the boundaries of previously restored parts and locating hidden metallic components connecting the architectural elements. Information on the internal structure and spatial distribution of metallic junctions was essential for gaining insight into building techniques in order to discriminate between restoration strategies which may require either total or partial dismantling of the rose window. GPR results provided crucial evidence in favour of one of the (conflicting) hypotheses about the original building techniques, leading to the selection of partial dismantling as the most suitable restoration strategy. Analysis of measurements revealed the potential of GPR in the field of cultural heritage restoration, even in those cases characterized by complex geometry, structural brittleness and logistic difficulties, such as that discussed in this paper.

## INTRODUCTION

Architectural restoration requires a detailed study of materials, building techniques and state of preservation. The cultural value and fragility of historical monuments limit or prevent the use of destructive techniques, and non-destructive testing (NDT) methods are being increasingly used (McCann and Forde 2001). Ground-penetrating radar (GPR) is one of the geophysical methods that have been successfully applied to cultural heritage and civil engineering investigations (Davis and Annan 1989; Conyers and Goodman 1997). Non-destructive imaging, fast data acquisition and high resolution enable the detection of centimetre-scale targets with high spatial accuracy to depths of several tens of centimetres (Ulriksen 1982; Binda *et al.* 1998).

Successful applications of GPR, often integrated with other geophysical techniques (e.g. sonic tests, seismics, electrical resistivity), include bridge (Scott *et al.* 2003) and channel side-wall assessment (Francese *et al.* 2004), diagnosis of masonry structures (Valle and Zanzi 1998) and void and fracture detection (Valle *et al.* 1999). In the field of cultural heritage, shallow geophysical techniques are usually applied in archaeological prospecting (Sambuelli *et al.* 1999; Basile *et al.* 2000; Piro *et al.* 2003; Chianese *et al.* 2004; Seren *et al.* 2004) and in the diagnosis of historical architectural elements, such as walls, columns, pillars and vaults (Cardarelli 1995; Maierhofer and Leipold 2001; Cardarelli *et al.* 2002; Ranalli *et al.* 2004).

The use of GPR for the investigation of historical buildings

---

* luigina.nuzzo@unile.it

requires an accurate knowledge of the electromagnetic properties of the building materials. As is known, neglecting the influence of magnetic permeability (nearly equal to that of vacuum in most natural materials), the propagation, absorption and reflection of the electromagnetic waves depend on the complex electric permittivity of the investigated media (see Appendix). As it is one of the main constituents of both natural and artificial materials, water plays an important role in GPR investigations. Many authors have focused on the development of theoretical models and the experimental determination of the dielectric properties of wet materials or water-saturated rocks (Shen *et al*. 1985; Taherian *et al*. 1990; Wensink 1993). In contrast, apart from concrete (Robert 1998), only a few papers have reported on measurements of the complex permittivity of building materials (dry or wet) in the frequency range of interest for GPR (Maierhofer *et al*. 1998; Sambuelli *et al*. 1998; Vaccaneo *et al*. 2004). Studies in frequency ranges higher than the GPR range (Maierhofer and Wöstmann 1998), especially for wireless communications, appear more frequently in the literature. Therefore, there is still a need for intensive investigations into the electromagnetic properties of building materials in the GPR frequency band in order to obtain more quantitative information from GPR surveys.

This paper discusses the results of a geophysical survey using GPR performed on the rose window of the Troia Cathedral, one of the most famous medieval artefacts in southern Italy (Belli D'Elia 1998). As a consequence of past seismic events, the upper part of the façade underwent rotational strains, which caused cracks in the architectural elements of the rose window. In order to preserve the historical monument, a preliminary study suggested two different kinds of restoration technique (Liberatore and Masini 2004). The first one consists of dismantling the whole rose window followed by reassembly. The second one consists of an *in situ* structural reinforcement, supported by a partial dismantling of the architectural elements. To evaluate which of the two restoration methods is better, detailed knowledge of the materials, the original building techniques and the structural damage was necessary. For this objective, we used GPR to investigate the internal structure of the rose window and to detect the iron bolts connecting the architectural elements.

## THE ROSE WINDOW
### Architectural elements
Troia is an ancient town in the north-west part of Apulia. It is renowned for its beautiful cathedral (Fig. 1a) constructed between the 11th and 13th centuries (Belli D'Elia 1998). The cathedral's rose window (Fig. 1b) is one of the most famous medieval artistic works in southern Italy. It was built in the second half of the 13th century as a decorative feature of the upper part (tympanum) of the main façade. The rose window (Fig. 1b), is a large circular window with a diameter of 6.60 m. The window consists of two symmetrical structures of wheel rays, one on the inside and the other on the outside of the cathedral. Eleven twin columns (Fig. 1b) radiate from a central oculus and are joined by means of capitals to a stone ring composed of trapezoidal elements decorated with intersecting arched ribwork (Fig. 1b). Triangular panels with geometric-motif tracery enrich the spaces between the columns (Fig. 1b). The wheel window is joined to the masonry by means of a circular ashlar curb (Fig. 1b).

### Building materials
A mineralogical and petrographic study provided evidence of the different materials used (Calia 2004). In particular, the carved triangular panels are composed of medium-to-fine-grained calcarenites, the oculus is made of fine-grained limestone and the elements with intersecting arches are made of coarse-grained calcarenites (Fig. 1c). Finally, the ashlar curb is composed of two main kinds of material, light-coloured calcarenites and greenish sandstones. The external columns (Fig. 1c) are made of re-used white marble with grey stripes (the so-called "Proconnesio" marble, in columns 1, 2, 4), white marble with grey spots ("Pentelico" marble in column 9), white-marble breccia ("Pavonazzetto" in columns 6 and 10), green-grey sandstone (in column 3), white-greyish compact limestone (in column 5),
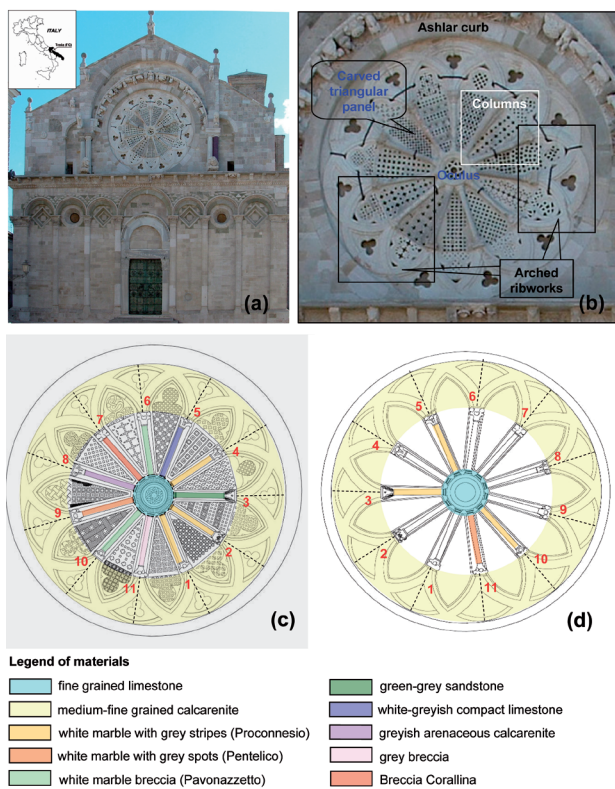


FIGURE 1
(a) Picture of the Romanesque façade of Troia Cathedral, Apulia, Italy (inset). (b) Close-up of the rose window with the architectural elements discussed in the next figures highlighted. (c) Overview of the building materials used for the various architectural elements of the rose window superimposed on the drawings of the external. (d) Drawings and building materials of the internal façade.
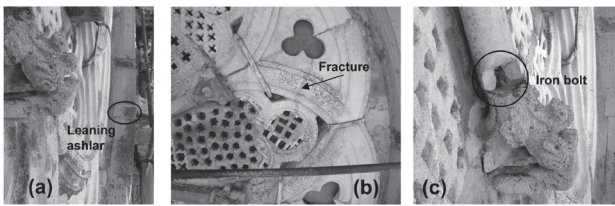
FIGURE 2

(a) Out-of-plane deformations and a leaning ashlar visible from a lateral view of the ashlar curb. (b) Mortar-filled fracture on arched ribwork. (c) Detachment of marble at the base of a column revealing the presence of an iron anchor bolt in the capital.
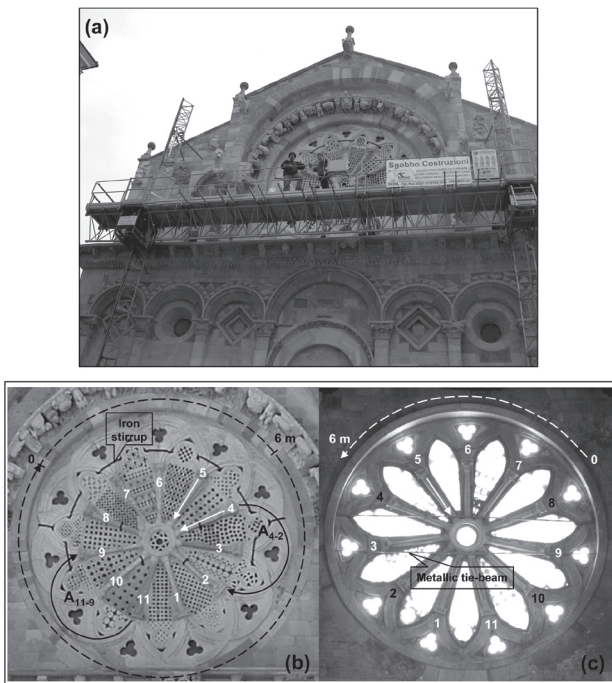


FIGURE 3

(a) Picture of the twin-mast climber used during data acquisition on the external façade. (b) External and (c) internal views of the rose window and layout of the GPR profiles recorded with 1500 MHz (white lines) or both 900 and 1500 MHz antennae (black lines) along the ashlar curb (dashed), the arched ribwork (solid, black) and the columns (white). Columns numbered in black were not surveyed. Only the profiles discussed in the next figures are shown.

calcareous breccia with a reddish ferruginous-clayey matrix ("Breccia Corallina" in column 7), greyish arenaceous calcarenite (in column 8) and calcareous breccia with brown-greyish matrix (in column 11). Because of their heterogeneous composition, different responses to the electromagnetic investigation are therefore expected. On the inner side of the rose window (Fig. 1d), the columns are more homogeneous. They are made mainly of Proconnesio marble (columns 3, 5 and 10) and Pentelico marble (column 11). Most of them are covered with a thin layer of plastering, which prevents a precise identification of the assumed marble constitution.

**State of preservation**

The state of preservation of the rose window is mainly conditioned by its structural deflections. In particular, the photogrammetric survey revealed the loss of perfect verticality of the plane of the rose window and the noticeable out-of-plane strains at some ashlars in the circular curb (Fig. 2a). As a consequence of past seismic events, such as the 1731 earthquake, the upper part of the façade underwent rotational strains which caused cracks and detachments in the architectural elements (Fig. 2b,c). In some cases, the detachment of small pieces revealed the presence of iron bolts and fused lead joining the architectural elements (Fig. 2c). Because of these structural problems, some restoration work has been carried out since the second half of 19th century (Picone 2000). Unfortunately this work has not prevented the strains from progressing and further structural restoration is still necessary to preserve this historical window.

The rotation of the façade induced severe deformation and damage in the rose window, which is displaced outwards in the upper part and inwards at the centre. Disconnection and rotation of the capitals, as well as compression failures of the columns can be seen. Relative displacements, up to 1 cm, can also be observed at the joints between the arched ribwork. This suggested that the possibility of dismantling some of the elements of the rose window (in particular, the columns) in order to reinforce and reassemble them should be considered.

**GPR SURVEY STRATEGY AND DATA ACQUISITION**

The design of the most effective restoration procedure requires a correct diagnosis of the problems, and an accurate knowledge of building characteristics and of all the parameters defining the structural model, such as internal and external constraints. For these reasons, the GPR survey aimed to

- determine the thickness and internal structure of the circular curb;
- detect cracks in the columns and the calcarenite elements with intersecting arches;
- find the iron bolts in joints between columns and capitals, and between columns and the central oculus;
- delineate the boundaries between the restored parts and the original materials.

On the external side, the complex geometry of the rose window and the elevation from the ground surface (about 15 m) required the use of a twin mast-climber (Fig. 3a) and specific geophysical acquisition techniques. Fixed scaffolding was used for the survey on the internal side. The GPR measurements were performed on different architectural elements of the wheel window, along the external (Fig. 3b) and internal (Fig. 3c) façades. On the external side, due to the large diameter of the rose window (about 6 m), several adjacent profiles were carried out along the circular ashlar curb for a total length of about 20 m (Fig. 3b).
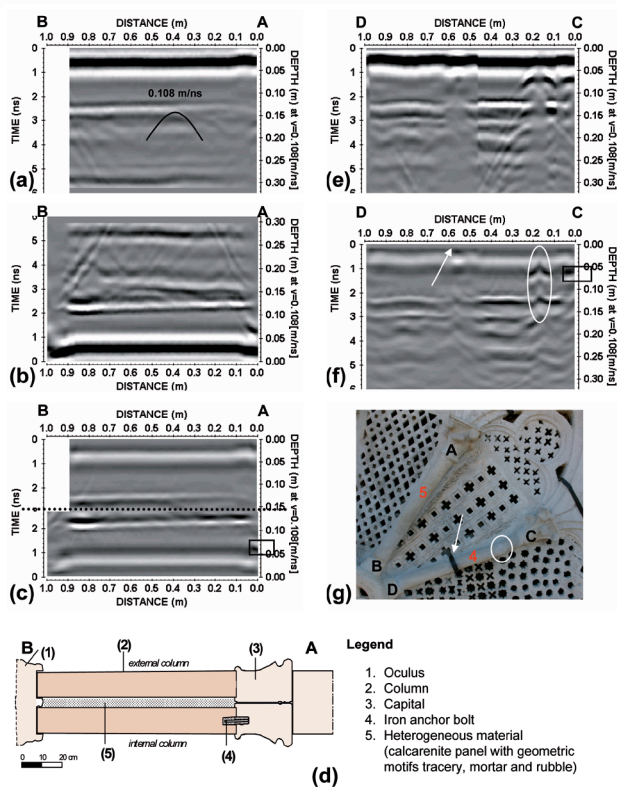
**FIGURE 4**

Example of GPR results (1500 MHz) on the columns (Fig. 3). (a) and (b) Unmigrated radargrams on the external and the internal columns 5 and velocity estimation by fitting a diffraction hyperbola. (c) Composite image for the twin columns 5 obtained using the shallowest portion of external and internal migrated sections. (d) Architectural interpretation of columns 5. (e) Unmigrated and (f) migrated radargrams on the external column 4. (g) Picture of columns 5 and 4. Black rectangles in (c) and (f) denote the interpreted position of iron anchor bolts; white arrows in (f) and (g) denote a metallic stirrup; white ellipses in (f) and (g) mark superficial cracks.

**TABLE 1**

Summary of the main acquisition parameters for the GPR survey

| Architectural element | Range | Antenna | Band-pass filters |
|---|---|---|---|
| Circular ashlar curb | 30 ns | 1500 MHz | 250 – 3000 MHz |
| | | 900 MHz | 100 – 1800 MHz |
| Arched shape ribwork | 15 ns | 1500 MHz | 250 – 3000 MHz |
| | | 900 MHz | 100 – 1800 MHz |
| Columns | 6 ns | 1500 MHz | 250 – 3000 MHz |

Dense reference markers (every 0.5 m) along the middle circumference, a partial overlap of consecutive profiles and accurate field notes were necessary to minimize positioning errors in the location of traces along the circular resulting profile (see Results section). In addition, 11 radargrams along the intersecting arched ribwork and 11 radargrams along the columns were acquired (Fig. 3b). On the internal side, because of the presence of fixed scaffolding and two metallic tie-beams on the inner façade, only the upper part of the circular ashlar curb (about 6 m) and some columns were investigated (Fig. 3c). A SIR2000 instrument (GSSI), with 900 and 1500 MHz antennae in continuous mode, was used. The acquisition parameters are summarized in Table 1. For each antenna, the acquisition filters were selected in order to reduce low- and high-frequency noise while preserving enough bandwidth (at least three octaves of the nominal frequency) to guarantee good resolution. Manual gain was also applied to obtain the best visualization *in situ*.

## DATA PROCESSING

Data were processed using ReflexW software (Sandmeier 2004). The processing flow included trace editing, spatial resampling to 0.01 m trace intervals, acquisition gain removal and zero-time correction. For both the ashlar curb and the intersecting arched ribwork, a background removal filter was applied in the first few nanoseconds to remove direct arrivals and enhance shallow lateral discontinuities. High-frequency noise was attenuated by means of a 2D average filter (by taking the average of the data inside an $x$–$t$ moving window of $3 \times 3$ points). The known thickness of the architectural elements (10 to 12 cm for the columns, 26 cm for the intersecting arches and 66 cm for the ashlar curb) and diffraction hyperbolae in the data provided two ways of estimating the average electromagnetic-wave velocity. These velocities were used for 2D Kirchhoff migration and depth conversion. As an example, in Fig. 4(a), a velocity of 0.108 m/ns is estimated to fit one of the diffraction hyperbolae located just below the flat reflection from the back of the external column 4. This value is in good agreement with the velocity obtained by dividing the column thickness (11 cm) by the one-way time of the corresponding reflection.

Regarding the velocity analysis on the columns, slight variations from 0.104 to 0.112 m/ns were found for the external columns according to the different materials, as shown in Table 2. The statistical analysis of the velocity values gives an average of 0.109 m/ns with a standard deviation of 0.002 m/ns. The highest velocity of 0.112 m/ns was found in the sandstone column 3 and the lowest value of 0.104 m/ns in the Breccia Corallina and the Pentelico marble (respectively columns 7 and 9). The investigated columns of the internal façade show electromagnetic-wave velocity values in the same range (0.104– 0.112 m/ns), but with a lower average value (0.107 m/ns) and a higher standard deviation (0.004 m/ns).

Relatively constant values were obtained from the velocity analysis on the intersecting arched ribwork and along the ashlar curb. Their average velocities were 0.104 m/ns and 0.098 m/ns, respectively.

**TABLE 2**
Materials and electromagnetic velocity values of external and internal columns

| Column no. | External | | Internal | |
|---|---|---|---|---|
| | Material | velocity (m/ns) | Material | velocity (m/ns) |
| 1 | white marble with grey stripes (Proconnesio) | 0.110 | marble? | 0.104 |
| 2 | white marble with grey stripes (Proconnesio) | 0.110 | marble? | |
| 3 | green-grey sandstone | 0.112 | white marble with grey stripes (Proconnesio) | 0.104 |
| 4 | white marble with grey stripes (Proconnesio) | 0.108 | marble? | |
| 5 | white-greyish compact limestone | 0.108 | white marble with grey stripes (Proconnesio) | 0.108 |
| 6 | white marble breccia (Pavonazzetto) | 0.110 | marble? | 0.112 |
| 7 | Breccia Corallina | 0.104 | marble? | 0.112 |
| 8 | greyish arenaceous calcarenite | 0.108 | marble? | |
| 9 | white marble with grey spots (Pentelico) | 0.104 | marble? | 0.104 |
| 10 | white marble breccia (Pavonazzetto) | 0.110 | white marble with grey stripes (Proconnesio) | |
| 11 | grey breccia | 0.108 | marble with quartz (Pentelico) | 0.104 |
| **Average** | | 0.108 | | 0.107 |
| **Standard deviation** | | 0.002 | | 0.004 |

## RESULTS

### Columns

As stated above, the rose window is characterized by two symmetrical column sets. The 11 columns of the external set (Fig. 1c) consist of different materials (Table 2) and have slightly different diameters (10–12 cm). Presumably all the internal columns are made of marble of probably poorer quality. A layer, 3–5 cm thick, of inhomogeneous material separates the internal and external columns. In this space, the carved panels are joined together by rubble and mortar. Thus, the thickness of the three-layer medium (external column - inhomogeneous material - internal column) is about 26 cm. The low-loss materials (mostly marble and calcarenites) enable the 1500 MHz antenna to probe the entire three-layer structure. Profiles were acquired from the capital towards the central oculus from both sides of the rose window (Fig. 3b,c). Columns indicated with black numbers in Fig. 3(c) were not surveyed, because of the presence of obstacles.

Figure 4 shows the results of columns 5 (both internal and external) and 4 (external only). The abscissa axis of the radargrams is reversed to approach the orientation of the columns in the picture (Fig. 4g). The unmigrated radargram acquired along column 5 from the external side (Fig. 4a) clearly shows a horizontal, variable-amplitude reflection from the boundary between the column and the intermediate layer, at about 2.4 ns. The absence of diffractions or reflections above this reflection is indicative of homogeneous material. The heterogeneous constitution of the layer between the columns is supported by the presence of weak diffraction hyperbolae. These hyperbolae mask a weaker reflection at about 3 ns, corresponding to the boundary between the inhomogeneous layer and the inner column. Furthermore, the air interface between the inner column and the interior of the cathedral is clearly visible as a relatively strong event at about 5 ns.

Figure 4(b) shows the unmigrated radargram obtained along column 5 from the inner side. To facilitate comparison with the previous figure, the radargram is plotted upside down. The lowering of the first reflector from 2.2 to 1.9 ns (from A, near the capital, to B, near the oculus) suggests a tapering of the inner column towards the oculus. The material of the inner column (white marble with grey stripes) appears to be homogeneous.

A strong semi-hyperbola with apex at 0.05 m and 1.2 ns is associated with the edge of an iron anchor bolt linking the column with the capital. The anchor bolt penetrates into the column for about 5 cm, as seen in the migrated section (Fig. 4c). Diffractions from the column edges are probably responsible for the semi-hyperbolae with apexes corresponding to the first reflector at both ends of the section. As before, the inhomogeneous layer is marked by weak diffraction hyperbolae. In this case, lower attenuation in the marble of the inner column explains the better visibility of the deeper reflectors, corresponding to the two boundaries of the external limestone column (Fig. 4b). Figure 4(c) is a composite view of both exterior and interior migrated cross-sections merged between the columns. The top halves of each GPR profile were rearranged so as to give the clearest image. Figure 4(d) shows a sketch of the section across the twin columns with the interpreted bolt within the capital.

Both unmigrated and migrated data for column 4 are shown in Fig. 4(e and f) respectively. The external column is made of white marble with grey stripes (Fig. 4g). A crack and an iron stirrup are visible. They are easily identified in the radargrams as strong diffraction at 0.17 m and superficial reflection at 0.45–0.60 m, respectively. The shadow zones behind these superficial features interrupt the continuity of later reflections, so that no clear information can be derived about the inner column. The shadow zone between the hyperbolic branches, caused by the crack edges, suggests heavy absorption probably due to the presence of mortar, attributed to past restorations. The hyperbolic branches at later times could indicate the continuation of the fracture into the inner column. This hypothesis is consistent with similar mechanical stresses supported by both columns. The presence of an iron anchor bolt joining the column to the capital (Fig. 4f) is visible as a diffraction hyperbola at the beginning of the unmigrated section.

**Intersecting arched ribwork**

The columns are joined through capitals to trapezoidal elements decorated by intersecting arched ribwork composed of homogeneous well-cemented calcarenites (Fig. 1c,d). Consequently, an almost constant velocity value (0.104 m/ns) was estimated from all radargrams. Each GPR profile was carried out along a semi-circular path spanning two adjacent panels and named after the columns they join (Fig. 3b). Two examples of 1500 MHz pre-processed and migrated data for the ribwork $A_{4-2}$ and $A_{11-9}$ are shown in Fig. 5.

In Fig. 5(a), relating to $A_{4-2}$, background removal in the first 2 ns enhances very shallow lateral discontinuities, such as those at 0.2–0.3 m and 1.0–1.1 m due to the iron stirrups (Fig. 5b,c). Moreover, the hyperbolic diffraction at the junction of the two panels (1.88 m), and also the anomalies at 2.4–2.6 m and 3.0–3.5 m, caused respectively by the corrugated surface and a longitudinal crack ($x$–$y$ in Fig. 5b,c), are clearly noticeable. The arch–air reflection is clearly visible at about 5 ns along the whole section. Between 1.88 and 2.40 m, a clear horizontal reflection at 3 ns

(about 13 cm) is visible. This is attributable to a calcarenite block inserted in previous restoration works. The hyperbola at the end of the profile at about 2.4 ns is probably due to an iron anchor bolt. Finally, hyperbolae below the arch–air reflection, with apexes at 1.40 and 1.88 m (Fig. 5b), are due to metallic tie-beams on the inner side of the rose window. It is worth noting that the fracture $f$ (Fig. 5b,c) is not easily recognizable on the radargram at 0.55 m, where only a minor lateral change in traveltime and amplitude of the air reflection is visible.

Figure 5(d) refers to profile $A_{11-9}$ and shows a rather different situation from the previous one. Stronger lateral variability across the two panels, both in internal texture and absorption properties, is noticeable. In particular, the reflection associated with the arch–air interface of the second panel is slightly deeper and shows a noticeably lower amplitude than that in the first panel. This result suggests a lower electromagnetic velocity and higher electrical conduction losses inside the material of the second panel, which is probably due to a local increase in moisture content because of condensation on the internal side of the wheel window. The same features previously discussed are visible, i.e. the superficial anomaly of the metallic stirrup (3.5 m), the diffraction from the tie-beam (3.6 m and 5 ns) and diffraction hyperbolae due to the iron anchor bolts with the capitals both at the beginning and at the end of the section. The flat reflector bordered by diffractions at 2.8 ns and discontinuities in the arch–air interface at 1.20 and 1.88 m identify the sharp limits of
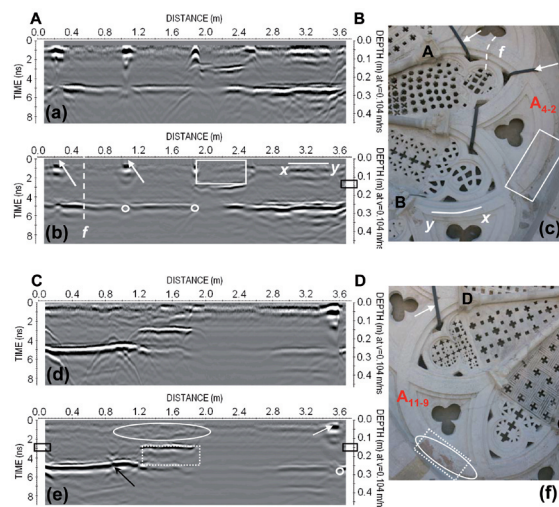


FIGURE 5

Example of GPR results (1500 MHz) on the intersecting arched ribwork (Fig. 3). (a) Unmigrated and (b) migrated sections on A4-2. (c) Picture of A4-2. (d) Unmigrated and (e) migrated sections on A11-9. (f) Picture of A11-9. White arrows denote metallic stirrups and white small circles mark metallic tie-beams on the inner side of the rose window. Black rectangles denote iron anchor bolts. The white line $x$–$y$ marks a longitudinal crack and line $f$ marks a mortar-filled fracture. White rectangles denote stone blocks inserted in previous restoration work. White ellipses mark natural rock variation. The black arrow indicates a possible defect in the rear part.
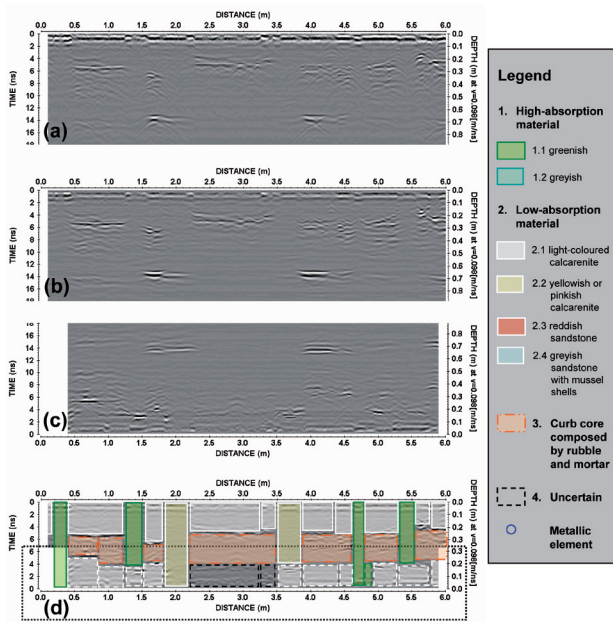
**FIGURE 6**

Example of GPR results (1500 MHz) on the circular ashlar curb from 0 to 6 m (Fig. 3). (a) Unmigrated and (b) migrated radargrams from the outer side. (c) Upside-down migrated radargram from the inner side. (d) Interpreted curb structure superimposed on the composite migrated section from both sides, outlining the ashlars' geometry and materials and revealing a more heterogeneous masonry core.

an anomalous zone. This anomaly can be interpreted as a 13 cm thick restored block at the back of the arched ribwork, not visible from the surface. The hyperbolic feature at 0.9 m, which collapses to a point-like zone at 3.5 ns and disrupts the continuity of the arch–air reflection in the migrated section (Fig. 5e), could be caused by a crack in the rear part.

The analysis of the radargrams from the other arcs outlined the presence of iron anchor bolts, generally at both ends although not always clearly evident. Taking into account the antenna dimensions and the fact that after migration the hyperbolae collapsed just at the borders of the radargrams or even outside, the length of the metallic anchor bolts inside the ribwork is estimated to be less than 10 cm. Finally, other features revealed by GPR were fractures, discontinuities attributable to old restoration work, natural heterogeneities and variations in the internal texture of the panels.

**Ashlar curb**

In order to understand how the wheel window is linked to the façade masonry, the circular ashlar curb was investigated along its whole circumference using 900 and 1500 MHz antennae from the external side, but only along the topmost 6 m using a 1500 MHz from the internal side (Fig. 3b,c). The GPR profiles were acquired in continuous mode with reference markers every 0.5 m. On the external side, several consecutive clockwise profiles of varying

lengths were acquired. To limit positioning errors and edge effects, each profile was collected with a partial overlap of 0.5 m with the previous one. After careful editing and removal of extra trace ranges and before applying multitrace operations, such as 2D filters and migration, which are prone to border effects, the various profiles were merged into a single radargram.

Despite a slight decrease in reflector continuity with respect to the 900 MHz survey, the 1500 MHz sections were preferable for interpretation, because of better resolution and enough signal penetration to investigate the whole of the masonry. Figure 6 shows examples of radargrams along the topmost 6 m of the ashlar curb from the external (unmigrated and migrated) and internal (migrated, displayed upside down for better comparison) sides, as well as the section interpreted on the basis of analysis of radar facies and comparison with the macroscopic elements and lithologies of the external ashlars.

The unmigrated section (Fig. 6a) clearly shows very shallow hyperbolic diffractions (collapsed to sharp lateral discontinuities in the migrated section of Fig. 6b) in good correspondence with the observed position of the mortar joints between the ashlars. The ashlars show different electromagnetic behaviours. Some of them are delimited by a strong flat basal reflector usually at 4–5 ns, whereas in other cases no reflection is recorded due to presumably higher absorption losses. The first reflection is generally followed by chaotic diffraction patterns revealing a heterogeneous intermediate layer in the masonry core, probably composed of rubble. The final reflection from the interface between the internal ashlar and air is observable at about 14 ns in a few low-absorption zones.

Time fluctuations of the reflection from the back side highlight velocity variations (with respect to the average velocity of 0.098 m/ns) due to different material characteristics, whereas amplitude differences are related to variable attenuation properties. The highest attenuation is noted for the greenish sandstone ashlars, where no reflections are recorded. The best characteristics in terms of homogeneity and transparency to the electromagnetic energy correspond to white, yellowish or greyish fine-grained calcarenitic ashlars. Some ashlars appear as well-squared blocks, on average 20 cm deep, whereas others seem to have rough-hewn inner faces. Small lateral and, mostly, vertical dimensions, such as for the ashlar between 5.55 and 5.75 m (Fig. 6b), could be an indication of a restored piece.

Medium-to-high-amplitude reflections from the curb–air interface (Fig. 6b) suggest the presence of squared blocks with rather good characteristics, similar to the white-yellowish ashlars, also in the back side (Fig. 6c). The high-amplitude curb–air reflection between 1.85 and 2.20 m and the absence of internal reflections indicate the presence of a good-quality cross ashlar, the so-called diaton, inserted crosswise in the masonry with the function of a connection between the internal and the external rows of the curb. By analogy, at 3.50–3.80 m, a 50 cm thick cross ashlar could be interpreted as a 'half-diaton', which links the external row to the core of the curb (Fig. 6b,c). Although the high
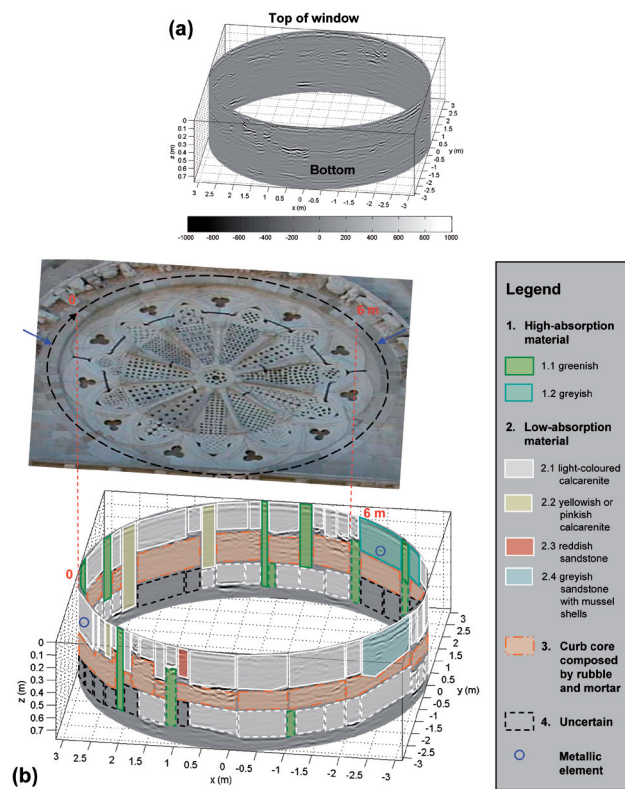
FIGURE 7

(a) 3D rendering of the 1500 MHz migrated radargram on the whole circular ashlar curb. (b) Perspective view of the rose window and interpreted curb structure superimposed on the migrated section. Blue arrows indicate the locations of point diffractors (blue circles) interpreted as metallic anchor bolts connecting the ashlar curb to the overhanging structure.

attenuation prevents the recording of any reflections, it is likely that the greenish sandstone ashlars, which usually have quite small lateral dimensions, were used as diatons or half-diatons. Finally, highly attenuating inner ashlars and core material can be hypothesized when no air reflection is visible after the first reflection and/or central diffraction pattern, such as between 2.25 and 3.50 m (Fig. 6b,c).

Because of attenuation and a decrease in lateral resolution with increasing time, acquisition from both sides of the masonry is needed in order to obtain the most complete information achievable from GPR investigations. Indeed, the migrated radargram from the inner side (Fig. 6c) helps to identify the lateral and depth limits of the inner ashlars. They appear generally less regular and thinner, at least for the investigated upper part of the curb. The presence of 10–15 cm thick inner pieces at 1.30–1.55 m and 5.25–5.75 m (Fig. 6c) helps to discriminate greenish ashlars used as half-diatons from those that probably cross the whole of the masonry.

Figure 6(d) shows the interpreted curb structure superimposed on the composite radargram obtained by merging the top-

most halves of the migrated sections from the external and the internal sides (Fig. 6b,c). As explained in the legend, based on the electromagnetic properties derived from GPR analysis, the curb materials were grouped into four classes and, in their turn, were divided into further subclasses according to aspect and lithological characteristics.

Using an in-house MATLAB program (The MathWorks 2002) to account for the cylindrical symmetry, the migrated radargram of the whole ashlar curb is rendered as a curved shape in Fig. 7(a) and interpreted in Fig. 7(b) on the basis of the above classification. The small lateral dimensions and the absence of internal reflections confirm the hypothesis that the highly absorbing greenish sandstones (class 1.1) were preferably used as diatons. The most populated class 2.1 includes light-coloured (calcarenitic) stones having the best electromagnetic characteristics and the most regular geometry (well-squared blocks); the smallest ashlars are probably restored pieces. Some of the inner ashlars were ascribed to classes 1.1 or 2.1, because of their electromagnetic behaviour (high absorption or presence of flat reflection) analogous to the outer ashlars of the corresponding classes.

The 3D visualization allows a better appreciation of the spatial relationships. In particular, two point-like diffractions (circles in Fig. 7b) are located inside the two largest ashlars close to the beginning of the overhanging sculptured arch (arrows in Fig. 7b), corresponding exactly with the places where the main failures and rotational strains occurred. The absence of similar anomalies in the nearby arched ribwork suggests that these anomalies could be due to a metallic anchor bolt connecting the curb to the outer sculptured arch.

## DISCUSSION
### Review of the results
In this section, the main results of the GPR survey on the Romanesque rose window of Troia Cathedral are summarized and discussed. GPR analysis led to the geometrical and the material characterization of the internal structure of the circular ashlar curb, through comparison of the radar response with the macroscopic elements and lithologies of the external ashlars. In particular, both external and internal rows appear to be composed of variably sized and well-squared ashlars of two main types: light-coloured calcarenites and greenish sandstones.

In Fig. 8, three radar traces are shown together with their amplitude spectra. Data were processed as described above. Moreover, they were compensated for spherical divergence before migration. The selected traces refer to three different situations. The first trace (blue in Fig. 8a) is from a zone (2.0 m in Fig. 6) interpreted as a single light-coloured calcarenitic ashlar, because of the strong air reflection at 13 ns and the absence of internal reflection. The second trace (green in Fig. 8a) is from a zone (4.0 m in Fig. 6) interpreted as two light-coloured calcarenitic ashlars separated by a more heterogeneous core, because of the very strong air reflection at 13 ns and the weak

internal reflections between 5 and 10 ns. The third trace (red in Fig. 8a) is from a zone (4.7 m in Fig. 6) interpreted as a single, highly attenuating, greenish sandstone, because of the very difficult identification of any reflection, even at the air interface. The air reflection is slightly anticipated in the green trace and, although hardly recognizable, seems slightly delayed in the red trace with respect to the blue trace. Because of the constant masonry thickness, this fact indicates a local increase in average velocity, i.e. a decrease in dielectric constant, in the three-layer case (green) and a local decrease in average velocity, i.e. increase in dielectric constant, in the greenish sandstone case (red), with respect to the homogeneous calcarenitic ashlar (blue). These variations in time, and hence in dielectric constant, can be related to variations in water content. According to the Topp relationship (Topp *et al*. 1980), the volumetric water content appears to increase from the green to the blue to the red trace. The spectra of the three traces (Fig. 8b) show clear differences in amplitude and shape. The amplitude spectrum of the trace at 4.0 m is the highest and widest, whereas the very small amplitude spectrum of the trace at 4.7 m is attributable to the high attenuation of the greenish sandstone. The spectra, each normalized to its respective maximum and expressed in dB (Fig. 8c), show that the peak frequency is at about 1200 MHz, which is lower than the nominal frequency, for the traces at 2.0 and 4.0 m, but the second spectrum decreases less slowly. The spectrum of the trace at 4.7 m is considerably rougher, although with almost the same bandwidth and peak frequency as the other traces.

The sandstone ashlars are more prone to meteoric degradation and, according to the spectral analysis of radar traces shown above, produce heavy absorption of the electromagnetic energy. They were employed as diatons or half-diatons to link the two



FIGURE 9

Spectral analysis of selected traces on the arched ribwork A11_9 (Fig. 5). From above: (a) Traces at 0.5 m (blue), 2.5 m (green) and 3.0 m (red). (b) Amplitude spectra of traces in (a). (c) Amplitude spectra each normalized to its respective maximum and expressed in dB.

circular rows. Their absence in the lower part of the curb (Fig. 7b) could give remarkable insights into the building stages of the rose window. GPR revealed a heterogeneous composition of the curb core, interpreted as rubble and mortar used to fill the space where the elements decorated by intersecting arch motifs are inserted. The ashlar curb appears to be connected to the overhanging structure by two symmetrically located metallic anchor bolts.

In the case of calcarenitic elements with arched ribwork, GPR revealed the presence of restored pieces involving either the front (Fig. 5b) or the back (Fig. 5e) side of the arch or its whole thickness. Lateral variations or local disruptions of the air reflection could be indicative of small cracks, not visible from the surface. The analysis of reflection or diffraction patterns, as well as attenuation properties, allowed us to gain insights into different textures or decay states of the same material. For instance, variable wave velocity or absorption could be related to variable moisture content, due either to water seepage or to vapour condensation on the internal side of the wheel window.

As an example, Fig. 9 shows the spectral analysis of three radar traces from the arched ribwork $A_{11\_9}$ (at 0.5, 2.5 and 3.0 m in Fig. 5e,f). The traces shown in Fig. 9(a) were compensated for spherical divergence before migration. The air reflection (at about 4.7 ns) has noticeable amplitude variations from the trace at 0.5 m (high) to the trace at 2.5 m (very low) and the trace at 3.0 m (low). In addition to the highest attenuation, the air reflection at 2.5 m (green) also shows a slight time delay, which suggests a local increase in water content. The corresponding spectra (Fig. 9b) show clearly that the amplitude decreases and the bandwidth becomes narrower from the left (trace at 0.5 m) to the right portion of the arch (2.5 m and 3.0 m). The difference is even more apparent in Fig. 9(c), where the spectra are normal-
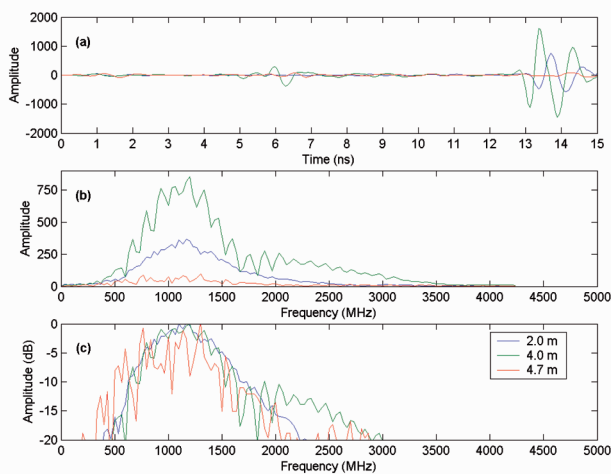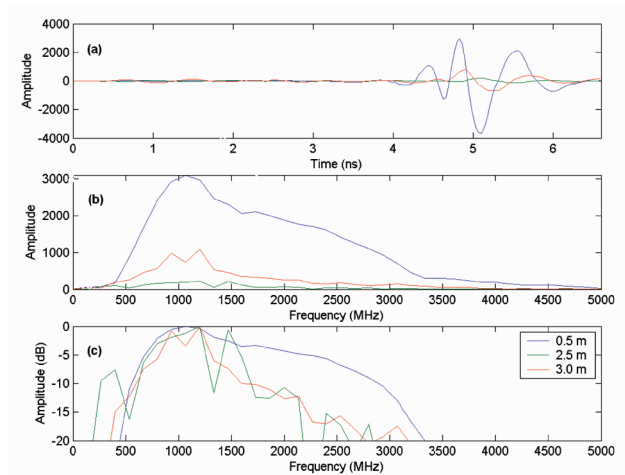


FIGURE 8

Spectral analysis of selected traces on the ashlar curb (Fig. 6). From above: (a) Traces at 2.0 m (blue), 4.0 m (green) and 4.7 m (red). (b) Amplitude spectra of traces in (a). (c) Amplitude spectra each normalized to its respective maximum and expressed in dB.
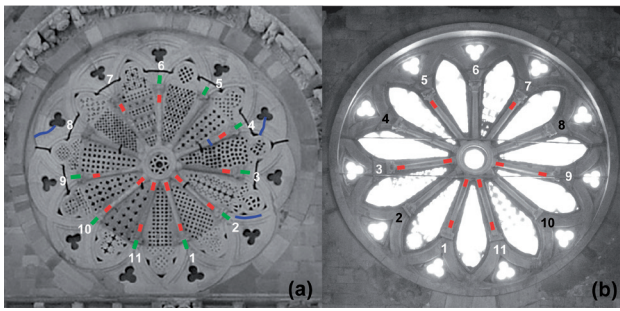
FIGURE 10
Synthesis of the main anomalies revealed by the GPR survey on (a) the external and (b) the internal sides of the rose window: iron anchor bolts within columns (red), iron anchor bolts within arched ribwork (green) and fractures (blue).

ized to their respective maxima and expressed in dB, and can be explained as materials with different attenuation properties in the two portions of the arched ribwork. Moreover, the slight amplitude increase from the trace at 2.5 m to the trace at 3.0 m, both in the right-hand portion, shows that lateral variations also exist inside the same material. Variable attenuation is attributable to subtle variations in the lithology, clay content and electrical conductivity of the pore fluids.

Figure 10 shows an overview of the main results obtained from the GPR survey on the columns and arched ribwork. Concerning the main objective, clear diffraction hyperbolae from iron anchor bolts were observed near the capital and also near the oculus for the external columns 1, 2, 10 and 11, located in the lower part of the rose window (Fig. 10a). Regarding the internal columns (Fig. 10b), the analysis of GPR measurements suggests the presence of iron anchor bolts at both ends for columns 1, 3, 9, 11, near the capital for columns 5 and 7, but none for column 6. This primary and *a priori* unexpected result provided valuable information about medieval building techniques. By detecting iron elements in both ends of the lower columns, and in one end of the upper columns, we were able to discover how the building of the rose window evolved. In the first phase, the lower columns were laid and the oculus was centred. Subsequently, the upper columns were inserted several centimetres into the cups of the oculus and were joined with the capitals by means of metallic bolts, fused lead and mortar. This allowed optimization of the building tolerance in length during the positioning of the columns of the upper rays of the wheel window.

Anchor bolts within the arched ribwork, joining it to the capitals, were detected at both ends of the majority of profiles (Fig. 10a). Shorter anchor bolts could probably be present in the two cases where GPR did not give a clear indication.

Longitudinal or transverse fractures visible from the surface were also detected by GPR (Fig. 10a). However, while clear diffraction patterns were noted for a mortar-filled crack inside a marble column (Fig. 4), only minor amplitude and time varia-

tions of the air-interface reflection were noted for a mortar-filled fracture inside a calcarenitic arched ribwork (Fig. 5). This fact can be explained by a higher dielectric contrast between mortar and marble than between mortar and calcarenite.

To sum up, GPR results confirmed the presence of numerous problems affecting the various architectural elements of the rose window and the urgency of restoration. Fortunately, the overall stability of the structure does not appear to be compromised, although it could be greatly improved by appropriate reconstruction work. Thanks to the detection of the metallic connections between the various parts and understanding of the original building techniques, the less invasive restoration strategy, involving only partial dismantling and reconstruction *in situ*, can be recommended.

**Suitability of the method in cultural applications**
Even more important than the amount of information provided for this specific task, this case study offered an invaluable opportunity to assess the advantages and limitations of the GPR method in the challenging field of cultural heritage preservation. The first limitation is related to accessibility and coupling problems. In our case, it was necessary to overcome some logistic problems related to the small dimensions and the curvature of the objects under investigation and their complex geometry and morphology. For instance, the very small dimensions of the columns and arched ribwork did not always allow perfect coupling of the antenna with the object surface. Moreover, the presence of overhanging decorative elements, such as rings or capitals, limited the extent of the architectural elements that could be investigated. Also, the profile curvature played a major role. To understand fully the spatial distribution of the anomalies, the complex geometry of the circular ashlar curb required particular care, both at the acquisition and in the subsequent processing and visualization stages.

A second crucial point is related to the electromagnetic properties of the building materials and the amount of contrast between targets and background. In fact, surprisingly clear data were obtained for low-absorbing materials, such as most of the marble columns, the calcarenitic arched ribwork and the light-coloured calcarenitic ashlars. In contrast, less reliable results were obtained for columns of other materials, such as sandstone and breccia, and very poor information was obtained about the greenish-sandstone ashlars because of high absorption losses. In spite of these limitations, anchor bolts hidden only few centimetres inside the architectural elements were detected, thanks to the wide aperture of the GPR antenna, causing the diffraction tails from the metallic ends to be recorded even when the antenna was not located directly above the anomaly source.

As stated in the Introduction, the main advantages of the GPR method for cultural applications rely on its non-destructive nature, its moderately cheap and fast data acquisition, and its high-resolution imaging of the internal structure. In the case studied, it took only two days to acquire the data and a few

months for data processing and interpretation. A particular advantage of the method is that, unlike other non-destructive testing techniques, which are able to furnish only average values of some physical properties or information related to a very thin superficial layer, in favourable conditions GPR can give information about elements, hidden at depth below the object surface, with high spatial resolution.

Based on the experience acquired in this particular application, it can be deduced that most civil and public buildings might benefit from application of the GPR method for structural assessment before restoration. Marble buildings or monuments are particularly suitable, since marble seems to be the material for which the method works best. However, the degree of suitability depends on the variety of marble and the degree of decay. Good-to-moderate results can be obtained on (dry) limestone and calcarenitic structures. Due to fast energy attenuation and signal scattering, the GPR method is hardly applicable on sandstone or heterogeneous masonry. It performs better on structures built with dielectric homogeneous materials.

The very high resolving power often required in cultural heritage applications demands even higher-frequency antennae than those used here. Indeed, this is an open research branch. It is known, however, that the goal of high resolution is difficult to achieve without sacrificing depth of penetration. Another point that needs to (and more probably can) be improved in the future is the development of positioning systems able to give the necessary spatial accuracy for architectural applications, also in case of complex geometries.

## CONCLUSIONS

This paper describes the main results of GPR investigations performed on the Romanesque rose window of the Cathedral of Troia, Southern Italy. As a consequence of past seismic events, the architectural elements of the wheel window show many cracks and distortions, thus making effective restoration work urgent. The GPR method was used to acquire detailed knowledge of the materials employed and the building techniques used, in order to evaluate the feasibility of restoration strategies which involve total or partial dismantling and reassembling of the building elements.

The complexity of the structure, the small dimensions of the objects under investigation and the variety of building materials employed, caused many logistic/coupling problems. Nevertheless, after careful data acquisition, processing, analysis and visualization of the results, the GPR survey was able to

• determine the internal structure of the circular ashlar curb;
• locate iron bolts connecting the various architectural elements;
• detect fractures and the boundaries of restored parts within columns and arched ribwork.

A noteworthy point is that imaging architectural elements with GPR from two sides (when possible) enabled better definition of the internal structure. As a consequence of the information gained through GPR, the restoration involving partial dismantling was judged to be the most suitable from both technical and economic points of view.

The results obtained were generally satisfactory and sometimes exceeded the *a priori* expectations. They show that GPR is a useful tool to analyse masonry structures from the geometrical, material and decay points of view, and also for cases characterized by complex morphology and building features, like the rose window of Troia Cathedral.

## REFERENCES

Basile V., Carrozzo M.T., Negri S., Nuzzo L., Quarta T. and Villani A.V. 2000. A ground-penetrating radar survey for archaeological investigations in an urban area (Lecce, Italy). *Journal of Applied Geophysics* **44**, 15–32.

Belli D'Elia P. 1998. Per la storia di Troia: dalla chiesa di S. Maria alla cattedrale. *Vetera Christianorum* **25**, 605–620.

Binda L., Lenzi G. and Saisi A. 1998. NDE of masonry structures: use of radar tests for the characterisation of stone masonries. *NDT&E International* **31**, 411–419.

Calia A. 2004. I materiali lapidei costituenti il rosone. In: *Indagini diagnostiche e indicazioni progettuali per il restauro della facciata e del rosone della cattedrale di Troia*. Technical report ( D. Liberatore and N. Masini).

Cardarelli E. 1995. 3D tomography of some pillars of the Coliseum. *Bollettino di Geofisica Teorica ed Applicata* **37**, 267–275.

Cardarelli E., Godio A., Morelli G., Sambuelli L., Santarato G. and Socco L.V. 2002. Integrated geophysical surveys to investigate the Scarsella vault of St. John's Baptistery in Florence. *The Leading Edge* **67**, 467–470.

Chianese D., D'Emilio M.G., Di Salvia S., Lapenna V., Ragosta M. and Rizzo E. 2004. Magnetic mapping, ground penetrating radar surveys and magnetic susceptibility measurements for the study of the archaeological site of Serra di Vaglio (Southern Italy*). Journal of Archaeological Science* **31**, 633–643.

Cole K.S. and Cole R.H. 1941. Dispersion and absorption in dielectrics. *Journal of Chemical Physics* **9**, 341–351.

Conyers L.B. and Goodman D. 1997. *Ground-penetrating Radar – An Introduction for Archaeologists*. Alta Mira Press, Walnut Creek.

Davis J.L. and Annan A.P. 1989. GPR for high-resolution mapping of soil and rock stratigraphy. *Geophysical Prospecting* **37**, 531–551.

Debye R. 1929. *Polar Molecules*. Dover Publications, Inc., Mineola, NY.

Francese R., Galgaro A. and Grespan A. 2004. Venice channel side-wall assessment with GPR technique - a case study. *Journal of Applied Geophysics* **56**, 31–40.

Jonscher A.K. 1977. The universal dielectric response. *Nature* **267**, 673–679.

Liberatore D. and Masini N. 2004. *Indagini diagnostiche e indicazioni progettuali per il restauro della facciata e del rosone della cattedrale di Troia*. Technical report.

Maierhofer C. and Leipold S. 2001. Radar investigation of masonry structures. *NDT&E International* **34**, 139–147.

Maierhofer C., Leipold S. and Wiggenhauser H. 1998. Investigation of the influence of moisture and salt content on the dielectric properties of brick materials using radar. *Proceedings of the 7th International Conference on Ground Penetrating Radar (GPR), Kansas, USA,* pp. 477–84.

Maierhofer C. and Wöstmann J. 1998. Investigation of dielectric properties of brick materials as a function of moisture and salt content using a microwave impulse technique at very high frequencies. *NDT & E International* **31**, 259–263.

McCann D.M. and Forde M.C. 2001. Review of NDT methods in the assessment of concrete and masonry structures. *NDT&E International* **34**, 71–84.

Picone R. 2000. 'Ristauro' e de-restauro. Il caso della cattedrale di Troia in Puglia. In: *Restauro Dalla Teoria alla Prassi* (ed. S. Casiello), pp. 76–102, Electa Napoli.

Piro S., Goodman D. and Nishimura Y. 2003. The study and characterization of Emperor Traiano's Villa (Altopiani di Arcinazzo, Roma) using high-resolution integrated geophysical surveys. *Archaeological Prospection* **10**, 1–25.

Ranalli D., Scozzafava M. and Tallini M. 2004. Ground penetrating radar investigations for the restoration of historic buildings: the case study of the Collemaggio Basilica (L'Aquila, Italy). *Journal of Cultural Heritage* **5**, 91–99.

Robert A. 1998. Dielectric permittivity of concrete between 50 MHz and 1 GHz and GPR measurements for building materials evaluation. *Journal of Applied Geophysics* **40**, 89–94.

Sambuelli L., Godio A., Guo T.J. and Socco L.V. 1998. Laboratory determination of the dielectric permittivity of building stones in the 0.2–6 GHz band. *IV Meeting of the Environmental and Engineering Geophysical Society (European Section), Barcelona, Spain*, Expanded Abstracts, pp. 477–480.

Sambuelli L., Socco L.V. and Brecciaroli L. 1999. Acquisition and processing of electric, magnetic and GPR data on a Roman site (Victimulae, Salussola, Biella). *Journal of Applied Geophysics* **41**, 189–204.

Sandmeier K.J. 2004. *REFLEXW, Version 3.0.8 Windows™ 9x/ NT- program for the processing of seismic, acoustic or electromagnetic reflection, refraction and transmission data.* Copyright 1998-2004 by K. J. Sandmeier, Zipser Straße 1, D- 76227 Karlsruhe, Germany. www.sandmeier-geo.de

Scott M., Rezaizadeh A., Delahaza A., Santos C.G., Moore M., Graybeal B. and Washer G. 2003. A comparison of nondestructive evaluation methods for bridge deck assessment. *NDT&E International* **36**, 245–255.

Seren S., Eder-Hinterleitner A., Neubauer W. and Groh S. 2004. Combined high-resolution magnetics and GPR surveys of the Roman town of Flavia Solva. *Near Surface Geophysics* **2**, 63–68.

Shen L.C., Savre W.C., Price J.M. and Athavale K. 1985. Dielectric properties of reservoir rocks at ultra-high frequencies. *Geophysics* **50**, 692–704.

Taherian M.R., Kenyon W.E. and Safinya K.A. 1990. Measurement of dielectric response of water-saturated rocks. *Geophysics* **55**, 1530–1541.

The MathWorks, 2002. MATLAB Version 6.5.0.

Topp G.C., Davis J.L. and Annan A.P. 1980. Electromagnetic determination of soil water content: measurements in coaxial transmission lines. *Water Resources Research* **16**, 574–582.

Ulriksen P. 1982. *Application of impulse radar to civil engineering.* PhD thesis, Lund University of Technology, Lund, Sweden.

Vaccaneo D., Sambuelli L., Marini P., Tascone R. and Orta R. 2004. Measurement system of complex permittivity of ornamental rocks in L frequency band. *IEEE Transactions on Geoscience and Remote Sensing* **42**, 2490–24.

Valle S. and Zanzi L. 1998. Traveltime radar tomography for NDT on masonry and concrete structures. *European Journal of Environmental Engineering Geophysics* **2**, 229–246.

Valle S., Zanzi L. and Rocca F. 1999. Radar tomography for NDT: comparison of techniques. *Journal of Applied Geophysics* **41**, 259–269.

Wensink 1993. Dielectric properties of wet soils in the frequency range 1–3000 MHz. *Geophysical Prospecting* **41**, 671–696.

## APPENDIX

### Principles of electromagnetic-wave propagation

The propagation, absorption and reflection of GPR signals depend on the constitutive parameters of the media in which they propagate. The most important parameter is the complex electric permittivity $\varepsilon$, which consists of an in-phase component $\varepsilon'$ and an out-of-phase component $\varepsilon''$, and is in general a function of the frequency $f$ (or the angular frequency $\omega = 2\pi f$):

$$\varepsilon(f) = \varepsilon'(f) - i\varepsilon''(f). \tag{A1}$$

The imaginary part of the permittivity, $\varepsilon''$, is associated with the energy dissipation, and the real part of the permittivity, $\varepsilon'$, is associated with the capability to store energy when an alternating electrical field is applied. Often a relative quantity is used, the complex relative dielectric permittivity or the complex dielectric constant $\varepsilon_r$, defined as

$$\varepsilon_r = \frac{\varepsilon}{\varepsilon_0} = \varepsilon_r' - i\varepsilon_r'', \tag{A2}$$

where $\varepsilon_0 = 8.854 \times 10^{-12}$ F/m is the free space electric permittivity.

The second constitutive parameter is the conductivity, which can be approximated by a real parameter $\sigma' = \sigma_{dc}$, equal to the dc conductivity, since the high-frequency component is generally negligible. The third parameter is the magnetic permeability $\mu$, normally expressed as the product of the free-space magnetic permeability, $\mu_0 = 4\pi \times 10^{-7}$ henry/m, and the relative magnetic permeability $\mu_r$. Most geological materials are non-magnetic, so that $\mu_r$ is taken to be unity except where metallic objects or minerals are present in abundance.

The propagation of electromagnetic (EM) waves in a medium is governed by Maxwell's equations. Useful approximations for describing the propagation of radar signals can be found by considering the time harmonic solution of the scalar wave equation, derived from Maxwell's equation for the case of a homogeneous isotropic medium. In good conductors, the scalar equation reduces to a diffusion equation, and the fields do not propagate as EM waves. For materials with low conductivity, and when the frequency of the oscillating electric field is high enough, the displacement current dominates over the conduction current, and electromagnetic waves will propagate. The electric field $E$ at a distance $z$ and time $t$ can then be written as

$$E(z,t) = E_0 e^{-\alpha z} e^{i(\omega t - \beta z)}. \tag{A3}$$

Equation (A3) is the expression for a damped plane wave propagating with phase velocity

$$v = \frac{\omega}{\beta}, \tag{A4a}$$

and having a wavelength

$$\lambda = \frac{2\pi}{\beta} = \frac{v}{f}. \tag{A5}$$

The quantities

$$\alpha = \omega\sqrt{\mu\varepsilon'}\left\{\frac{1}{2}\left[\sqrt{1+\tan^2\delta}-1\right]\right\}^{1/2} \tag{A6}$$

and

$$\beta = \omega\sqrt{\mu\varepsilon'}\left\{\frac{1}{2}\left[\sqrt{1+\tan^2\delta}+1\right]\right\}^{1/2}, \tag{A7}$$

are the attenuation constant and the phase constant, respectively, while

$$\tan\delta = \frac{\sigma_e}{\omega\varepsilon'} = \frac{\sigma'+\sigma\varepsilon''}{\omega\varepsilon'} \tag{A8a}$$

is the loss tangent, which represents the ratio of conduction current density to displacement current density. It depends on the effective conductivity $\sigma_e$ and includes both the conduction losses $\sigma'$, which dominate at low frequencies, and the dielectric losses $\omega\varepsilon''$, due to relaxation phenomena, which dominate at high frequencies.

Using equations (A1) and (A2), the propagation velocity of EM waves, $v$, and loss tangent, $\tan\delta$, can be rewritten as

$$v(f) = \frac{c}{\sqrt{\varepsilon_r'(f)\mu_r\frac{1+\sqrt{1+\tan^2\delta}}{2}}}, \tag{A4b}$$

$$\tan\delta = \frac{\frac{\sigma'}{2\pi f\varepsilon_0}+\varepsilon''(f)}{\varepsilon'(f)}, \tag{A8b}$$

where

$$c = \frac{1}{\sqrt{\varepsilon_0\mu_0}} \cong 3\times10^8 \text{ m/s is the electromagnetic velocity in free space.}$$

Where GPR is most effective, the loss tangent is very small $(\tan\delta \ll 1)$, and media are non-magnetic $(\mu \cong \mu_0)$. In this case, the attenuation and phase constants reduce to

$$\beta \cong \frac{\omega}{c}\sqrt{\varepsilon_r'}, \tag{A9}$$

$$\alpha \cong \frac{Z_0}{2}\frac{\sigma_e}{\sqrt{\varepsilon_r'}}, \tag{A10}$$

where

$$Z_0 = \sqrt{\frac{\mu_0}{\varepsilon_0}} = 376.8\ \Omega \text{ is the free-space intrinsic impedance.}$$

In the usual GPR frequency band (10–1000 MHz), for geological materials with conductivities below 50 mS/m (all but clay), the propagation velocity depends exclusively on the real part of the dielectric constant and is not frequency dependent:

$$v \cong \frac{c}{\sqrt{\varepsilon_r'}}, \tag{A11}$$

and the medium attenuation can be approximated by

$$\alpha \cong \frac{1.69\times10^3\sigma'}{\sqrt{\varepsilon_r'}} \text{ dB/m,} \tag{A12a}$$

where $\sigma'$ is in units of S/m (Davis and Annan 1989). It is worth noting that, for a perfect dielectric $(\sigma'=0)$, there is no attenuation: i.e. $\alpha=0$. At high frequencies (above 1000 MHz), dispersion can occur because of water relaxation phenomena. In such cases, the dielectric losses can dominate over conduction losses $(\omega\varepsilon'' \gg \sigma')$ and the attenuation can be approximated by a different relationship:

$$\alpha \cong \frac{1.69\times10^3\omega\varepsilon_r''\varepsilon_0}{\sqrt{\varepsilon_r'}} \text{ dB/m.} \tag{A12b}$$

Sharp contrasts in dielectric permittivity or, more generally, impedance contrasts cause the reflection of EM waves. The intrinsic impedance $Z$ is given by

$$Z = \sqrt{\frac{i\omega\mu}{\sigma+i\omega\varepsilon}} = \sqrt{\frac{\mu}{\varepsilon'(1-i\tan\delta)}} = Z_0\sqrt{\frac{\mu_r}{\varepsilon_r'(1-i\tan\delta)}}. \tag{A13}$$

For two half-spaces separated by a flat interface, the reflection $(R)$ and transmission $(T)$ coefficients at normal incidence are given by

$$R = \frac{Z_2-Z_1}{Z_2+Z_1}, \tag{A14}$$

$$T = \frac{2Z_1}{Z_2+Z_1}, \tag{A15}$$

where $Z_i$ is the intrinsic impedance of the $i$th medium.

For low-loss $(\tan\delta \ll 1)$ non-magnetic media $(\mu \cong \mu_0)$, the intrinsic impedance can be approximated by $Z \cong \frac{Z_0}{\sqrt{\varepsilon_r'}}$ and the above coefficients can be expressed as a function of the relative permittivity or the velocity of the two media:

$$R = \frac{\left(\sqrt{\varepsilon_{r1}'}-\sqrt{\varepsilon_{r2}'}\right)}{\left(\sqrt{\varepsilon_{r1}'}+\sqrt{\varepsilon_{r2}'}\right)} = \frac{v_2-v_1}{v_2+v_1}, \tag{A16}$$

$$T = \frac{2\sqrt{\varepsilon_{r2}'}}{\left(\sqrt{\varepsilon_{r1}'}+\sqrt{\varepsilon_{r2}'}\right)} = \frac{2v_1}{v_2+v_1}. \tag{A17}$$

**Influence of water in GPR prospecting**

The complex permittivity of most materials varies considerably with the frequency of the applied electric field. An important process contributing to the frequency dependence of permittivity is the polarization arising from the orientation with the imposed electric field of molecules that have permanent dipole moments, such as water molecules. The mathematical formulation of Debye describes this process for pure polar materials (Debye 1929):

$$\varepsilon_r(\omega) = \varepsilon_\infty + \frac{\varepsilon_s - \varepsilon_\infty}{1 + i\omega\tau}, \tag{A18a}$$

which is equivalent to

$$\varepsilon_r(f) = \varepsilon_\infty + \frac{\varepsilon_s - \varepsilon_\infty}{1 + i\dfrac{f}{f_{rel}}}, \tag{A18b}$$

where $\varepsilon_\infty$ represents the permittivity at frequencies so high that molecular orientation does not have time to contribute to the polarization, and $\varepsilon_s$ represents the static permittivity (i.e. the value at zero frequency). The Debye formula assumes a single relaxation time, $\tau = \dfrac{1}{2\pi f_{rel}}$, where $f_{rel}$ is the relaxation frequency, defined as the frequency at which the permittivity equals $\dfrac{\varepsilon_s + \varepsilon_\infty}{2}$. Other formulae have been proposed, such as the Cole–Cole formula (Cole and Cole 1941), which assumes a distribution of relaxation times, and a 'universal' power-law relationship proposed by Jonscher (1977).

Equations (A18) shows that at frequencies that are very low and very high with respect to the relaxation frequency, the real part of the permittivity has constant values and the imaginary part is zero. At intermediate frequencies, the permittivity undergoes a dispersion: the real part of the permittivity decreases rapidly and dielectric losses occur with the peak loss at $f = f_{rel}$.

Liquid water is a prime example of a polar dielectric, characterized by $\varepsilon_s = 80.1$, $\varepsilon_\infty = 4.2$ and $f_{rel} = 10^{10.2}$ Hz (17.1 GHz) at 25°C. Whereas in sandy soils most water is in its free liquid state, in high clay-content soils, pore water is physically absorbed in capillaries. Dielectric relaxation of water absorbed on soil particles or clay minerals takes place at lower frequencies than the relaxation of free water. Dielectric relaxation phenomena are generally neglected in the frequency band 10–1000 MHz, normally used in GPR applications, but they can be important at frequencies above 1000 MHz, especially for clay-rich wet materials.

In the 10–1000 MHz frequency band, the real part of the relative permittivity is about 3 to 10 for most dry geological constituents, whereas it is approximately 80 for water and 1 for air. This large permittivity contrast explains the success of GPR in the determination of water content or the detection of voids. Classical theoretical approaches which relate the bulk permittivity of a soil-air-water mixture to the individual permittivity of each constituent are based on dielectric mixing models, such as the complex refractive index model (CRIM). However, the most commonly used relationship between relative permittivity $\varepsilon_r$, estimated from the EM-wave velocity, and volumetric water content $\theta$, is due to Topp *et al.* (1980) and was determined empirically for mineral soils of various textures:

$$\theta = -5.3\times10^{-2} + 2.92\times10^{-2}\varepsilon_r' - 5.5\times10^{-4}\left(\varepsilon_r'\right)^2 + 4.3\times10^{-6}\left(\varepsilon_r'\right)^3. \tag{A19}$$